

Plasmonic lens enhanced mid-infrared quantum cascade detector

Andreas Harrer, Benedikt Schwarz, Roman Gansch, Peter Reininger, Hermann Detz, Tobias Zederbauer, Aaron Maxwell Andrews, Werner Schrenk, and Gottfried Strasser

Citation: *Applied Physics Letters* **105**, 171112 (2014); doi: 10.1063/1.4901043

View online: <http://dx.doi.org/10.1063/1.4901043>

View Table of Contents: <http://scitation.aip.org/content/aip/journal/apl/105/17?ver=pdfcov>

Published by the *AIP Publishing*

Articles you may be interested in

[Thermal properties of mid-infrared colloidal quantum dot detectors](#)

J. Appl. Phys. **110**, 033110 (2011); 10.1063/1.3619857

[Heterojunction plasmonic midinfrared detectors](#)

J. Appl. Phys. **109**, 043108 (2011); 10.1063/1.3548896

[Integrated plasmonic lens photodetector](#)

Appl. Phys. Lett. **94**, 083501 (2009); 10.1063/1.3086898

[Roomtemperature operation of midinfrared surfaceplasmon quantum cascade lasers](#)

AIP Conf. Proc. **893**, 1451 (2007); 10.1063/1.2730453

[InP-based quantum cascade detectors in the mid-infrared](#)

Appl. Phys. Lett. **88**, 241118 (2006); 10.1063/1.2210088



2014 Special Topics

PEROVSKITES | 2D MATERIALS | MESOPOROUS MATERIALS | BIOMATERIALS/ BIOELECTRONICS | METAL-ORGANIC FRAMEWORK MATERIALS

AIP | APL Materials

Submit Today!

Plasmonic lens enhanced mid-infrared quantum cascade detector

Andreas Harrer,^{a)} Benedikt Schwarz, Roman Gansch, Peter Reininger, Hermann Detz, Tobias Zederbauer, Aaron Maxwell Andrews, Werner Schrenk, and Gottfried Strasser
Institute for Solid State Electronics and Center for Micro- and Nanostructures, Vienna University of Technology, 1040 Vienna, Austria

(Received 27 August 2014; accepted 23 October 2014; published online 30 October 2014)

We demonstrate monolithic integrated quantum cascade detectors enhanced by plasmonic lenses. Surface normal incident mid-infrared radiation is coupled to surface plasmon polaritons guided to and detected by the active region of the detector. The lens extends the optical effective active area of the device up to a 5 times larger area than for standard mesa detectors or pixel devices while the electrical active region stays the same. The extended optical area increases the absorption efficiency of the presented device as well as the room temperature performance while it offers a flexible platform for various detector geometries. A photocurrent response increase at room temperature up to a factor of 6 was observed. © 2014 Author(s). All article content, except where otherwise noted, is licensed under a Creative Commons Attribution 3.0 Unported License. [<http://dx.doi.org/10.1063/1.4901043>]

Mid-infrared (MIR) sources and detectors have attracted attention for several applications which lead to extensive research on that topic. Applications such as chemical fingerprinting, infrared imaging, and military countermeasure systems rely on integrated high performance photodetectors. Intersubband (ISB) devices are particularly interesting, as they cover the MIR spectral region with the characteristic absorption lines of many chemical compounds and offer high freedom in design with respect to their operation wavelength.

Beginning with the work of Kazarinov and Suris¹ in 1971 and the first demonstration of a quantum cascade laser (QCL) by Faist *et al.*,² the research field for intersubband sources was established. Intersubband detectors such as quantum well infrared photodetectors (QWIPs) have already proven their applicability and evolved to a wide range of efficient devices which include multi-wavelength megapixel focal plane arrays (FPA),³ THz devices,⁴ and photovoltaic QWIPs.⁵ When photovoltaic QWIPs were discovered and the light detection capability of QCL structures was shown by Hofstetter *et al.*⁶ the starting point for quantum cascade detector⁷ (QCD) research was set. Since then QCDs in the mid-infrared,⁸ near-infrared, and THz⁹ regions were demonstrated with significantly higher operating temperatures as known from QWIPs. Recently, an overall performance improvement by a diagonal transition design was reported.¹⁰ Beside separated MIR lasers and detectors, their on-chip integration based on a bifunctional quantum cascade laser detector (QCLD)¹¹ material has been demonstrated. Recently, a room temperature monolithic integrated MIR lab-on-a-chip using plasmonics with the capability to potentially reach ppm resolution over a widely varying concentration range was presented.¹²

The main requirements for ISB detectors are high responsivity, low noise, and normal incident sensitivity at room temperature. Apart from bandstructure optimization several methods have been shown to address these needs.

QWIPs¹³ and QCDs¹⁴ fabricated as photonic crystal slabs were demonstrated to exhibit enhanced detectivity by resonant absorption. Metal gratings¹⁵ and dielectric gratings are common ways to couple normal incident radiation to the active zone of FPA pixels. The field of plasmonics offers other options for source and detector enhancements. Plasmonic structures built of subwavelength apertures and surface corrugations have been used to collimate the emission beams of QCLs.¹⁶ Plasmonic lenses were shown to be applicable to metal-semiconductor-metal detectors in the near infrared.¹⁷

In this letter, we demonstrate a plasmonic lens QCD enabled for normal incident illumination respecting the ISB selection rules while the detector response is enhanced by an increased optical area. The detector mesa is surrounded by a metallic second order grating and a surface plasmon polariton (SPP) guiding region. Three device designs with different absorption lengths and polarization selectivities are demonstrated (Figure 1). Normal incident MIR radiation is coupled to the metal grating, where SPPs are excited and guided towards the QCD active zone. High end-fire coupling is achieved through an additional dielectric loaded SPP guiding region between the grating and the active region (Figure 2(a)). The optical area is extended by the plasmonic lens while the electric active mesa size stays small. As a consequence, the detector noise remains low, while the photocurrent is increased.¹⁸ This is particularly useful, if the MIR beam cannot be well confined, as it is the case for thermal sources.

The second order grating period p is designed to overcome the wavevector mismatch between the impinging radiation and the SPP propagating towards the detector mesa (Figures 2(a) and 2(b)). For an illumination wavelength of $\lambda = 6.5 \mu\text{m}$, a grating period of $6.4 \mu\text{m}$ was obtained by simulation. The grating depth h is 750 nm with a duty cycle of 50%. In contrast to plasmonic beam shaping in order to reduce the divergence angle of QCLs,^{16,19} the duty cycle and etch depth have to be chosen to minimize reflections, hence maximize the light coupling to the grating. The propagation

^{a)}Electronic mail: andreas.harrer@tuwien.ac.at



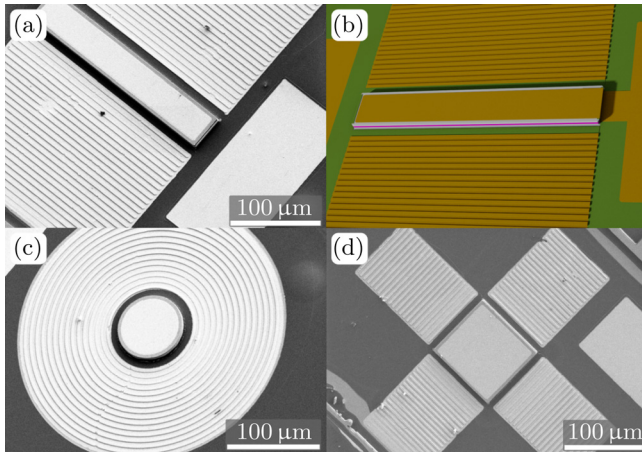


FIG. 1. Scanning electron microscope images and 3d illustration of plasmonic lens quantum cascade detectors with the active zone embedded in a dielectric waveguide surrounded by a second order (a) line grating; (b) line grating as 3d illustration with SiN covered gold SPP guiding region between the facet and the grating lens; (c) circular design; and (d) star shape design.

length L of the SPP is limited by the confinement of the mode on the gold/air, respectively, gold/SiN interface and ohmic losses. Thus the number of grating periods contributing to the detector signal is limited. Numeric simulations show a detector signal which scales linearly with a small number of periods (Figure 2(c)). The QCD response saturates for lenses with more than 15 periods. The 220 nm SiN layer on top of the gold of the guiding region increases the confinement of the SPP wave to the metal insulator interface.¹² The active region is embedded in a dielectric waveguide to increase the absorption length and thus the absorption efficiency. The spatial mode overlap is optimized via the thickness of the dielectric layer and the mesa etch depth.

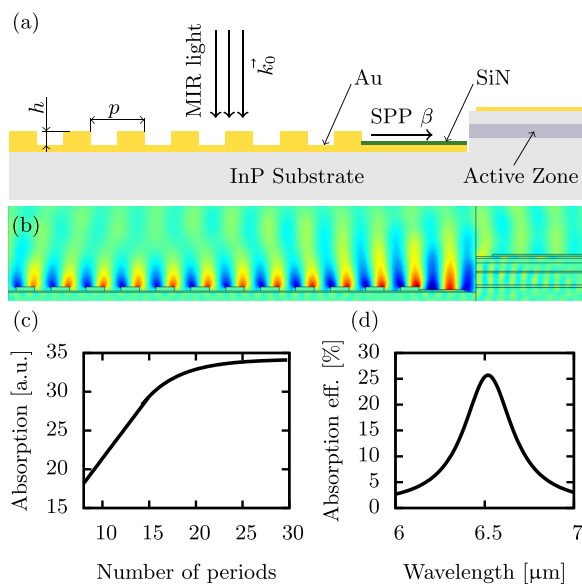


FIG. 2. Second order grating to couple incident radiation to surface plasmon polaritons. The grating parameters (a) have to be adjusted to overcome the wavevector mismatch between k_0 of the incident radiation and β of the propagating SPP. Optic simulation (b) of the electric field at the grating and coupling to the detector active zone with a fit (c) for the saturation of the absorption beginning at 15 periods and a maximum (d) spectral response at $6.5 \mu\text{m}$ for a grating period of $6.4 \mu\text{m}$.

All presented devices are processed from a bifunctional QCLD material¹¹ on InP substrate which offers the required waveguide for the active zone. In the first processing step, the detector mesa is structured by reactive ion etching. Then a layer of 750 nm SiN for the second order grating is deposited by plasma enhanced chemical vapor deposition. The deposited SiN thickness matches the desired grating depth. The grating is structured by photolithography and etched into the SiN layer followed by Ti/Au metallization of the lens. Subsequently, the ohmic Ge/Au/Ni/Au contacts are sputtered and the SiN guiding and isolation layers were deposited. The last metallization layer forms the Ti/Au extended contacts.

Figure 3 shows the room temperature performance of the three detector designs compared to a mesa detector illuminated through a polished 45° facet. For the star shape design and the line grating design, the photocurrent response is increased by approximately a factor of six and five, respectively, while the electrical active area is the same as for the mesa device. Although the circular shape detector has an electrical active mesa which is 2.6 times smaller than the 45° mesa it still has the same performance at 80 K as the reference device. At room temperature, the performance increase went up even to a factor of four. The increased response can be accounted for the enlarged optical area and the longer absorption length as a result of the coupling scheme. The absorption efficiency for the 45° mesa is given by $\eta \approx T_F(1 - e^{-\sqrt{2}\alpha L_{\text{Act}}})$, where α is the absorption coefficient, L_{Act} is the thickness of the active zone, and T_F the facet transmittance. For the SPP lens devices, the absorption efficiency is given by $\eta \approx \gamma_c(1 - e^{-\Gamma\alpha L_{\text{Mesa}}})$, where Γ is the mode confinement factor, γ_c the overall coupling efficiency and L_{Mesa} the waveguide length. Due to the longer absorption length $\Gamma L_{\text{Mesa}} \gg \sqrt{2}L_{\text{Abs}}$, the plasmonic lens devices have a higher absorption efficiency and a lower performance decrease with temperature. The signal drop between 80 K and room temperature is below 40% for the star shaped device (Figure 4). This is significantly lower compared to the 45° mesa devices. The line grating lens is designed for

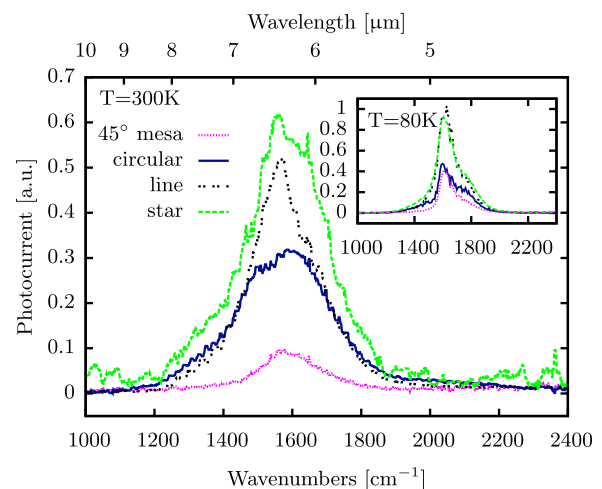


FIG. 3. Comparison of photocurrent responses for different plasmonic lens QCD device designs at room temperature. The line grating device and the star shaped device have the same detector mesa area as the 45° facet mesa ($100 \mu\text{m} \times 100 \mu\text{m}$) and exhibit a photocurrent increase up to a factor of 6. The circular design mesa is 2.6 times smaller than for the other two types. The inset shows the same devices at $T = 80 \text{ K}$.

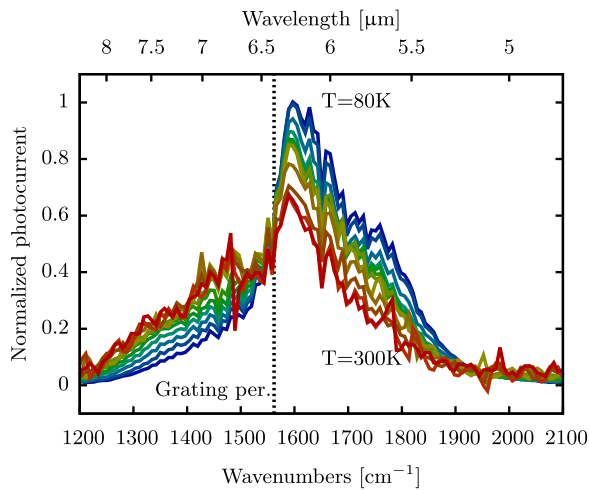


FIG. 4. Temperature dependent performance of a star shaped device for normal incident light. At the geometric grating period there is no pronounced peak visible due to the focused beam of the lens.

applications with QCL sources which emit linearly polarized light. The mesa dimensions are $250 \mu\text{m} \times 40 \mu\text{m}$ for the line grating device, $100 \mu\text{m} \times 100 \mu\text{m}$ for the star shape design as well as for the 45° mesa detector, and $\phi 70 \mu\text{m}$ for the circular detector. The higher performance of the star shape design can be described by its longer absorption length. Since all devices were measured without bias, hence in photovoltaic mode, there is no dark current contribution to the signal.

The grating coupling from free-space radiation was verified by polarization sensitive measurements of the line grating device (Figure 5). The photocurrent response of the detector was measured for different polarization directions of the impinging light. For increasing polarizer angles, a lower fraction of the impinging light is polarized with its electric field component perpendicular to the grating slits. Therefore, the photocurrent response drops with increasing angle. As the line grating device has the advantage of polarization sensitivity, it is suitable for applications, where selective detection is required. A combination of several sources and detectors with orthogonal polarization is possible to minimize optical crosstalk.

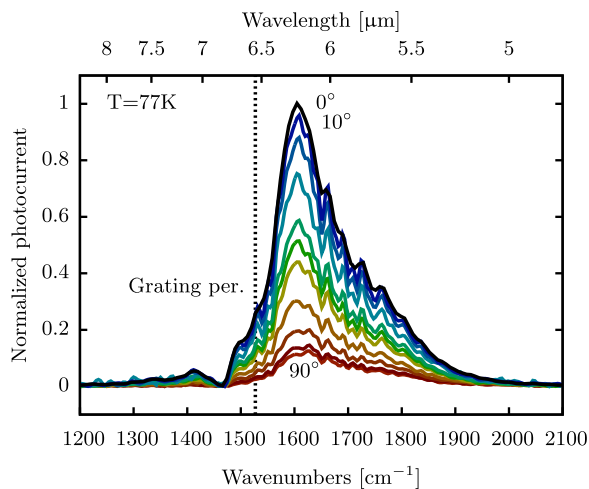


FIG. 5. Response of the plasmonic line grating device for different angles of linearly polarized light. The signal decreases with the angle differing from the favourable coupling direction of the electric field vector. The remaining detector signal for 90° is due to the efficiency of the used polarizer.

The plasmonic lenses were illuminated by a collimated global beam of a FTIR focused by a $f=5.08 \text{ cm}$ lens. The resulting distribution of angles of incidence on the grating allows to couple free space radiation around the design wavelength for normal incident light. Coupling in the entire spectral sensitivity range of the detector material can be expected.

Figure 6 shows the spatial intensity profile of a line grating device illuminated with a focused spectral narrow laser beam around $\lambda=6.6 \mu\text{m}$. The detector is moved over the laser spot with a linear stage while the detector response is measured. The laser light is linearly polarized with the electric field component perpendicular to the grating slits. For the line grating detectors, two maxima can be observed with a local minimum between the two peaks. This minimum is due to the detector mesa in the middle of the two lenses. As the mesa surface is covered with gold without grating the light is not coupled to the active zone in this region. The different detector response for the left and the right peaks is due to small processing imperfections. The spatial detector response can be modeled as the convolution of an illuminating Gaussian beam and a detector function accounting for the exponential decay of the SPP propagation on the lens. On the left and right hand side of the peaks, the detector response declines exponentially with increasing distance from the mesa facet. The decay is expressed by the

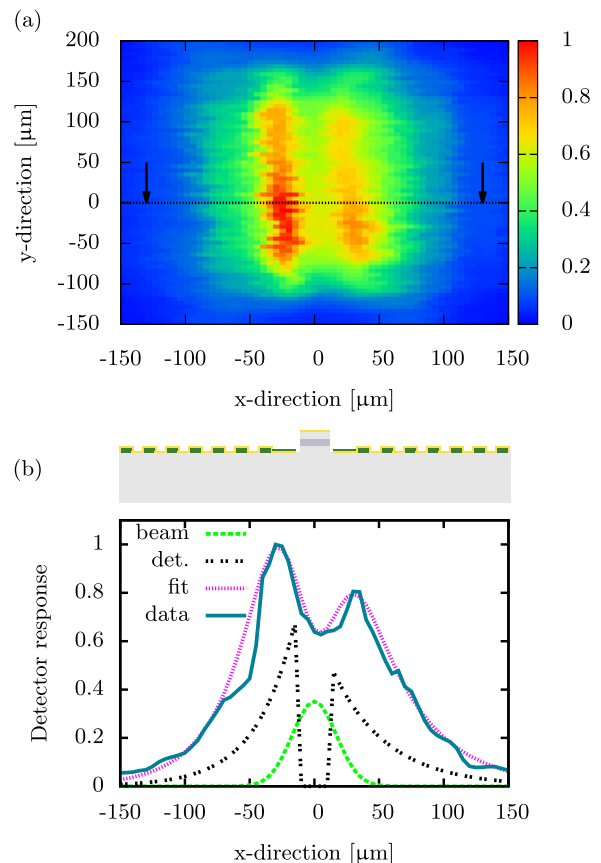


FIG. 6. Spatial detector signal (a) of a line grating device measured with a focused laser beam. The spatial resolution is $2 \mu\text{m}$. The local minimum is due to the detector mesa covered with gold where no coupling to the active zone is possible. (b) The spatial detector response as a cut line through the maximum in y -direction fitted as the convolution of a detector function with a Gauss beam. The surface plasmon propagation length extracted is $49 \mu\text{m}$.

propagation length L which is limited by ohmic and dielectric losses as well as re-radiation losses.

A propagation length of $49\ \mu\text{m}$ was extracted for the line grating devices. This corresponds to 7 grating periods (grating period $6.7\ \mu\text{m}$). The same behavior was observed in the simulations, where the response saturates above two times the propagation length, or 15 periods. Considering that the fraction of the optical area which effectively leads to an increased detector signal is limited by the propagation length. For the line grating device, a photocurrent increase by a factor of five was observed (Figure 3), which corresponds to the $2L$ limited optical area being 5 times the size of the 45° mesa detector. The devices should thereby be realized for a maximum of 15 periods which results in a higher performance per optical area.

In conclusion we designed, simulated, and fabricated plasmonic lens quantum cascade detectors in three different designs. All designs are sensitive for normal incident MIR radiation and work up to room temperature. The plasmonic lenses offer high geometric design flexibility and increased photocurrent responses up to a factor of six. The line grating type detectors are as a result of their polarization sensitivity the best choice for polarized light as from QCL sources. The star shape design shows the highest photocurrent increase by a factor of six and the circular design is the best choice for unpolarized light. With our work we have shown room temperature detectors with plasmonic lens enhanced absorption suitable for mobile sensing.

The authors acknowledge the support by the Austrian Science Fund in the framework of the Doctoral School "Building Solids for Function" (W1243) and the project NextLite (F4909-N23), as well as, by the PLATON project 35N within the Austrian NANO initiative and by the FP7 EU-project ICARUS.

- ¹R. F. Kazarinov and R. A. Suris, *Sov. Phys. Semicond.* **5**, 707 (1971).
- ²J. Faist, F. Capasso, D. L. Sivco, C. Sirtori, A. L. Hutchinson, and A. Y. Cho, *Science* **264**, 553 (1994).
- ³S. Gunapala, S. V. Bandara, J. Liu, J. Mumolo, D. Ting, C. Hill, and J. Nguyen, in *2009 IEEE Sensors* (IEEE, Christchurch, 2009), pp. 1609–1612.
- ⁴H. C. Liu, C. Y. Song, A. J. SpringThorpe, and J. C. Cao, *Appl. Phys. Lett.* **84**, 4068 (2004).
- ⁵H. Schneider, C. Schönbein, M. Walther, K. Schwarz, J. Fleissner, and P. Koidl, *Appl. Phys. Lett.* **71**, 246 (1997).
- ⁶D. Hofstetter, M. Beck, and J. Faist, *Appl. Phys. Lett.* **81**, 2683 (2002).
- ⁷L. Gendron, M. Carras, A. Huynh, V. Ortiz, C. Koeniguer, and V. Berger, *Appl. Phys. Lett.* **85**, 2824 (2004).
- ⁸M. Graf, N. Hoyler, M. Giovannini, J. Faist, and D. Hofstetter, *Appl. Phys. Lett.* **88**, 241118 (2006).
- ⁹F. Giorgetta, E. Baumann, M. Graf, Q. Yang, C. Manz, K. Kohler, H. Beere, D. Ritchie, E. Linfield, A. Davies, Y. Fedoryshyn, H. Jackel, M. Fischer, J. Faist, and D. Hofstetter, *IEEE J. Quantum Electron.* **45**, 1039 (2009).
- ¹⁰P. Reininger, B. Schwarz, H. Detz, D. MacFarland, T. Zederbauer, A. M. Andrews, W. Schrenk, O. Baumgartner, H. Kosina, and G. Strasser, *Appl. Phys. Lett.* **105**, 091108 (2014).
- ¹¹B. Schwarz, P. Reininger, H. Detz, T. Zederbauer, A. M. Andrews, S. Kalchmair, W. Schrenk, O. Baumgartner, H. Kosina, and G. Strasser, *Appl. Phys. Lett.* **101**, 191109 (2012).
- ¹²B. Schwarz, P. Reininger, D. Ristanić, H. Detz, A. Maxwell Andrews, W. Schrenk, and G. Strasser, *Nat. Commun.* **5**, 4085 (2014).
- ¹³S. Kalchmair, H. Detz, G. D. Cole, A. M. Andrews, P. Klang, M. Nobile, R. Gansch, C. Ostermaier, W. Schrenk, and G. Strasser, *Appl. Phys. Lett.* **98**, 011105 (2011).
- ¹⁴P. Reininger, B. Schwarz, A. Harrer, T. Zederbauer, H. Detz, A. Maxwell Andrews, R. Gansch, W. Schrenk, and G. Strasser, *Appl. Phys. Lett.* **103**, 241103 (2013).
- ¹⁵S. C. Lee, S. Krishna, and S. R. J. Brueck, *Opt. Express* **17**, 23160 (2009).
- ¹⁶F. Capasso, N. Yu, E. Cubukcu, and E. Smythe, *Opt. Photonics News* **20**, 22 (2009).
- ¹⁷J. A. Shackelford, R. Grote, M. Currie, J. E. Spanier, and B. Nabet, *Appl. Phys. Lett.* **94**, 083501 (2009).
- ¹⁸S. Krishna, S. Gunapala, S. Bandara, C. Hill, and D. Ting, *Proc. IEEE* **95**, 1838 (2007).
- ¹⁹N. Yu, R. Blanchard, J. Fan, Q. J. Wang, C. Pflugl, L. Diehl, T. Edamura, S. Furuta, M. Yamanishi, H. Kan, and F. Capasso, *IEEE Trans. Nanotechnol.* **9**, 11 (2010).